Contents lists available at ScienceDirect

Journal of Power Sources

journal homepage: www.elsevier.com/locate/jpowsour





Energetic variational approach for prediction of thermal electrokinetics in charging and discharging processes of electrical double layer capacitors

Xiang Ji^a, Chun Liu^b, Pei Liu^{c,d,*}, Shenggao Zhou^{e,**}

- ^a Department of Mathematics, Soochow University, 1 Shizi Street, Suzhou 215006, Jiangsu, China
- ^b Department of Applied Mathematics, Illinois Institute of Technology, Chicago, IL 60616, USA
- ^c School of Mathematics, University of Minnesota, Twin Cities, MN 55455, USA
- ^d Department of Mathematical Sciences, Florida Institute of Technology, Melbourne, FL 32901, USA
- e School of Mathematical Sciences, MOE-LSC, and CMA-Shanghai, Shanghai Jiao Tong University, Shanghai 200240, China

HIGHLIGHTS

- · First-principle prediction of thermal electrokinetics in supercapacitors.
- Generalization of steric Nernst–Planck equation to non-isothermal scenarios.
- · A temperature model based on the first and second law of thermodynamics.
- · Reversible and irreversible heat generation in charging and discharging processes.
- · CVT curve for cyclic voltammetry.

ARTICLE INFO

Keywords: Electrokinetics Electro-thermal coupling Energetic variation approach Cyclic voltammetry Modified Poisson-Nernst-Planck equations

ABSTRACT

This work proposes a new variational, thermodynamically consistent model to predict thermal electrokinetics in electric double layer capacitors (EDLCs) by using an energetic variational approach. The least action principle and maximum dissipation principle from the non-equilibrium thermodynamics are employed to develop modified Nernst–Planck equations for non-isothermal ion transport with temperature inhomogeneity. Laws of thermodynamics are employed to derive a temperature evolution equation with heat sources due to thermal pressure and electrostatic interactions. Numerical simulations successfully predict temperature oscillation in the charging–discharging processes of EDLCs, indicating that the developed model is able to capture reversible and irreversible heat generations. The impact of ionic sizes and scan rate of surface potential on ion transport, heat generation, and charge current is systematically assessed in cyclic voltammetry simulations. It is found that the thermal electrokinetics in EDLCs cannot follow the surface potential with fast scan rates, showing delayed dynamics with hysteresis diagrams. Our work thus provides a useful tool for physics-based prediction of thermal electrokinetics in EDLCs.

1. Introduction

Immense demand for green energy has greatly promoted the development of electrical energy storage technologies. Electric double layer capacitors (EDLCs), also known as supercapacitors, have received significant attention in recent years for their unique features and broad application spectrum [1]. Electric energy is stored in electric double layers forming at solid/liquid interface. In contrast to traditional dielectric capacitors, EDLCs can achieve much larger energy densities due to small charge separation in nanoscale electric double layers [2]. In contrast to conventional rechargeable batteries, EDLCs have higher

charging/discharging efficiency, longer cycle life, and higher power density [3–7].

The heat generation is a major concern for the function of EDLCs in that they are often cycled under high current density, which may result in an unexpected local temperature rise. In practice, excessive temperature rise in EDLCs could cause various irreversible damages, e.g., accelerated aging [8], enhanced self-discharge rates [9–11], capacitance reduction [12,13], and electrolytes decomposition/evaporation [14]. To avoid these issues, temperature elevation in EDLCs during operation should be suppressed. Therefore, comprehensive understanding on

E-mail addresses: xji@stu.suda.edu.cn (X. Ji), cliu124@iit.edu (C. Liu), pliu@fit.edu (P. Liu), sgzhou@sjtu.edu.cn (S. Zhou).

^{*} Corresponding author at: Department of Mathematical Sciences, Florida Institute of Technology, Melbourne, FL 32901, USA.

^{**} Corresponding author.

heat generation is of significance and highly desirable for the design, optimization, and manufacture of new generation EDLCs, to ensure the safety and long-term stability.

Temperature oscillations observed in the charging and discharging experiments of EDLCs evidence the contribution of the reversible and irreversible heat generation [5,15–17]. Many existing models on heat generation neglect the underlying thermal electrokinetic details in the operation of EDLCs. Either uniform heat generation for the whole device is assumed [10,16,18,19] or only irreversible heat generation is accounted for with parameters determined by experiments [5,10,20]. The irreversible Joule heating effect, which is proportional to the square of charge current, often accounts partially for the temperature change in EDLCs during charging and discharging processes [21–23]. Without reversible heat generation, theoretical models fail in predicting the temperature recession in the discharging process.

Much attention has been paid to the first-principle modeling of reversible and irreversible heat generation in EDLCs in recent years. Based on a thermodynamic viewpoint, Schiffer et al. [5] took into account the reversible heat generation rate as $-T\frac{dS}{dt}$, where the entropy change of ions due to the formation and dissolution of electric double layers is estimated by using the volume of Stern layers. The derived model can successfully predict the temperature oscillation in the charging-discharging processes. Zhang et al. proposed to describe the reversible heat via the relationship between surface Gibbs free energy and electric energy at the electric double layer interface [17]. Simulation results indicated that the proposed model could capture temperature oscillation during charging and discharging cycles and very well fit the experimental temperature profiles. To get physically faithful models with spatiotemporal resolution, d'Entremont et al. [24] developed an energy conservation equation for temperature, coupling electrodiffusion, heat generation, and thermal transport. The model incorporates irreversible Joule heating and reversible heat generation due to electrodiffusion, steric effect, and entropy changes. It is further extended to consider the effect of asymmetric ionic sizes on thermal and charge dynamics [22]. Numerical simulations demonstrated that the model is capable of predicting the temperature oscillation in charging-discharging processes. To reduce computational cost, scaling law analysis was performed to gain insights on reversible heating and develop a guideline for thermal management strategies [25].

Another type of model is derived by considering a source term that is the dot product of current and the electric field, including irreversible and reversible heat generation [23]. It is demonstrated that in terms of predicting the temperature change, the model has a good agreement with a thermodynamic identity involving temperature and electrostatics in the slow charging process. More recently, reversible heat production is studied based on a model that is derived by considering the ratio of reversible heat production into EDLCs during an isothermal charging process and the electric work [26]. It should be pointed out that the abovementioned models ignore porous structure of electrodes and treat EDLCs as a simple one-dimensional system with planar electrodes. Recent years have seen the development of models to evaluate the impact of cylindrical or porous electrodes on the performance of EDLCs [27-33]. For instance, a stack-electrode model with an electric circuit analogy was proposed to mimic the porous electrodes, and applied the model to study the relation between relaxation timescale and porosity [29,32]. The model was also extended to investigate the influence of structural parameters of porous electrodes on the temperature rise during the charging process of EDLCs [33].

Despite irreversible and reversible heat generations have been included, the abovementioned models describe ion transport by modified Nernst–Planck (NP) equations with ionic size effects [22,34–37], which ignore the impact of inhomogeneous temperature distribution on the ion transport as in isothermal scenarios. The effect of spatio-temporal inhomogeneity in temperature on charge dynamics is expected to become significant as large temperature rises in EDLCs [24]. Due to the

multi-scale and multi-physics nature, the development of thermodynamically consistent models for the charging/discharging processes of EDLCs has been a challenging issue.

In this work, we propose a variational, thermodynamically consistent model to predict thermal electrokinetics in EDLCs by using an energetic variational approach, which has been proved to be a powerful tool in studying numerous complex multi-scale, multi-physics systems [38], such as liquid crystals [39], multiple-phase flows [40], and ionic solutions [41]. The least action principle and maximum dissipation principle from the non-equilibrium thermodynamics are employed to derive modified NP equations that take into account the diffusion, ionic steric effect, and convection due to the gradient of temperature and electrostatic potential. Laws of thermodynamics are employed to derive temperature evolution equations with heat sources arising from thermal pressure and electrostatic interactions. Extensive numerical simulations based on the proposed model are performed to understand the thermal electrokinetics in the charging–discharging processes of EDLCs.

2. Methods

Consider a one-dimensional electric double layer capacitor (EDLC) that consists of binary, symmetric electrolytes blocked by two parallel electrodes located at x = -L - H and x = L + H; cf. a schematic plot of the system shown in Fig. 1. Hydrated cations and anions are assumed to have a uniform diameter a. With applied biased potential difference exerted by the electrodes, electric double layers due to electrostatic interactions are formed at electrodes. In electrolytes, a Stern layer right adjacent to each electrode is assumed to have width H = a/2, and it is followed by a diffuse layer. It is assumed that there is no electrochemical reaction at the interface between electrolytes and electrodes.

2.1. Energetic variational approach

We now propose an energetic variational model for the description of ionic electrodiffusion, heat generation, and thermal transport in EDLCs. Although a one-dimensional EDLC is mainly studied in present work, the model derived here is valid for general three dimensional cases.

To characterize the charging and discharging processes, we denote by T(x,t), $\psi(x,t)$, and $\rho_i(x,t)$ the temperature distribution, electric potential, and ionic concentration at location x for time t, respectively. Let Ω be the domain for an EDLC system under consideration. For any arbitrary subdomain $V \subset \Omega$, the mean-field electrostatic free-energy functional F(V,t) is a functional of the particle densities and temperature given by

$$F(V,t) = F_{pot}(V,t) + F_{ent}(V,t).$$
 (2.1)

Here the electrostatic potential energy reads

$$\begin{split} F_{pol}(V,t) &= \sum_{i,m=\pm} \frac{q_i q_m}{2} \iint_V \rho_i(\mathbf{x},t) \rho_m(\mathbf{x}',t) G(\mathbf{x},\mathbf{x}') d\mathbf{x} d\mathbf{x}' \\ &+ \sum_{i=\pm} q_i \int_V \rho_i(\mathbf{x}) \left(\psi_X(\mathbf{x},t) + \int_{\Omega \setminus V} \sum_{m=\pm} \rho_m(\mathbf{x}',t) G(\mathbf{x},\mathbf{x}') d\mathbf{x}' \right) d\mathbf{x}, \end{split} \tag{2.2}$$

where $q_i = z_i e$ with z_i being the ionic valence. The first term in $F_{pot}(V,t)$ represents for the electrostatic potential energy inside V from the Coulomb interactions, with the Green function G satisfying $-\nabla \cdot \epsilon_r \epsilon_0 \nabla G(\mathbf{x}, \mathbf{x}') = \delta(\mathbf{x}, \mathbf{x}')$. Here ϵ_0 is the absolute permittivity and ϵ_r is the dielectric coefficient. The second term is the electrostatic potential energy from the external fields, including contributions from ions outside V and an external electric potential ψ_X , e.g., the boundary

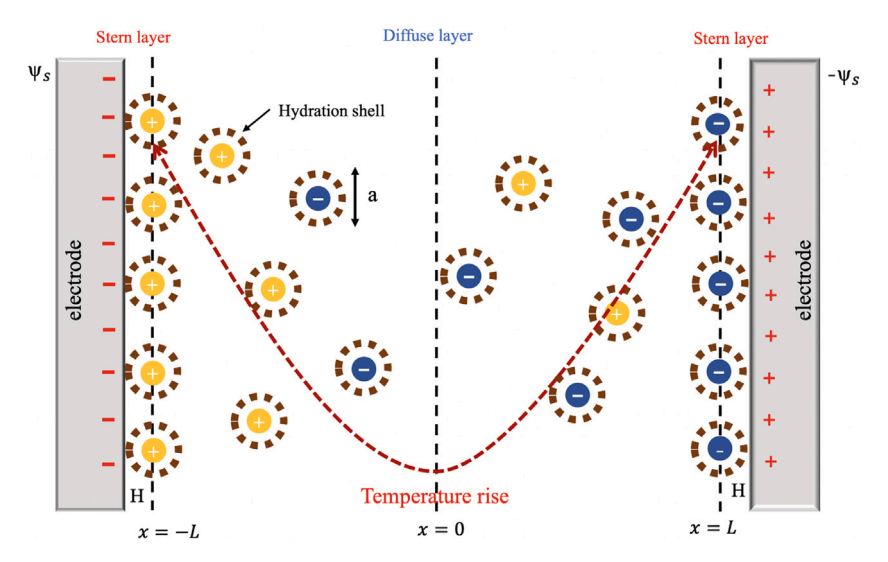


Fig. 1. A schematic view of an electric double layer capacitor. Hydrated cations and anions are assumed to have a uniform diameter a. Biased potential differences are applied across two thermally-insulated, blocking parallel electrodes that are located at x = -L - H and x = L + H with H being the width of Stern layers.

potential on the electrodes. The entropy contribution in (2.1) is given

$$F_{ent}(V,t) = \sum_{i=0,\pm} \int_V k_B T(\mathbf{x},t) \rho_i(\mathbf{x},t) [\log(v\rho_i(\mathbf{x},t)) - C_i \log T(\mathbf{x},t)] d\mathbf{x}, \tag{2.3}$$

where k_B is the Boltzmann constant and C_i is a constant related to the heat capacitance of each species. Note that the subscript i = 0stands for the solvent molecules, and uniform volume of both ions and solvent molecules, denoted by $v = a^3$, is assumed here. The steric effect is taken into account via the inclusion of solvent entropy, which is described by a lattice-gas model for uniform-sized solvent molecules and ions [42,43]. An upper limit 1/v is imposed on the local density via the constraint

$$\sum_{i=0,\pm} v \rho_i(\mathbf{x}, t) = 1. \tag{2.4}$$

For simplicity, we assume that $C_+ = C_- = C_0$ for each species. As such, the entropy contribution reads

$$\begin{split} F_{ent}(V,t) &= \int_{V} \Psi\left(\rho_{+}(\mathbf{x},t),\rho_{-}(\mathbf{x},t),T(\mathbf{x},t)\right) d\mathbf{x} \\ &\coloneqq \int_{V} \left[\sum_{i=\pm} \Psi_{i} \left(\rho_{i}(\mathbf{x},t),T\left(\mathbf{x},t\right)\right) \\ &+ \Psi_{0} \left(\rho_{+}(\mathbf{x},t),\rho_{-}(\mathbf{x},t),T(\mathbf{x},t)\right) - \Psi_{T}(T(\mathbf{x},t)) \right] d\mathbf{x}, \end{split}$$

where Ψ_+, Ψ_0 , and Ψ_T are defined as

$$\begin{split} \Psi_{\pm}\left(\rho_{\pm}(\boldsymbol{x},t),T\left(\boldsymbol{x},t\right)\right) &:= k_{B}T(\boldsymbol{x},t)\rho_{\pm}(\boldsymbol{x},t)\log\left(v\rho_{\pm}(\boldsymbol{x},t)\right),\\ \Psi_{0}\left(\rho_{+}(\boldsymbol{x},t),\rho_{-}(\boldsymbol{x},t),T\left(\boldsymbol{x},t\right)\right) \\ &:= k_{B}T(\boldsymbol{x},t)\frac{1-\sum_{i=\pm}v\rho_{i}(\boldsymbol{x},t)}{v}\log(1-\sum_{i=\pm}v\rho_{i}(\boldsymbol{x},t)), \end{split} \tag{2.5}$$

$$\Psi_T(T(\mathbf{x},t)) := \frac{k_B C_0}{t} T(\mathbf{x},t) \log T(\mathbf{x},t).$$

Then the entropy is given by

$$S(V,t) = -\int_{V} \frac{\partial \Psi\left(\rho_{+}(\mathbf{x},t), \rho_{-}(\mathbf{x},t), T(\mathbf{x},t)\right)}{\partial T(\mathbf{x},t)} d\mathbf{x}.$$
 (2.6)

Application of the Legendre transform of the free energy leads to the

$$U(V,t) = F(V,t) - \int_{V} T(\mathbf{x},t) \frac{\partial \Psi\left(\rho_{+}(\mathbf{x},t), \rho_{-}(\mathbf{x},t), T(\mathbf{x},t)\right)}{\partial T(\mathbf{x},t)} d\mathbf{x}.$$
 (2.7)

To characterize the thermal electrokinetics in EDLCs, we propose an energetic variational model that combines the non-equilibrium statistical mechanics and nonlinear thermodynamics [41,44,45]. Central in this model is the energy dissipation law

$$\frac{dE^{\text{tot}}}{dt} = -\Delta,\tag{2.8}$$

where $E^{\rm tot}$ is the total energy and the dissipation functional Δ often is a linear combination of the squares of various rate functions, such as velocity and rate of strain. In the energetic variational approach, the Least Action Principle (LAP) is used to derive conservative forces and the Maximum Dissipation Principle (MDP) is employed to obtain dissipative forces. The balance of total forces gives the governing equations for the motion of ions.

We first introduce the Lagrangian and Eulerian coordinate systems. Let Ω_0^X be the reference configuration and Ω_t^X be the deformed configuration of ions. Denote by $X \in \Omega_0^X$ the Lagrangian coordinate and $x \in \Omega^x$ the Eulerian coordinate. Introduce the flow maps that are

$$\frac{\partial}{\partial t} \mathbf{x}_{\pm}(\mathbf{X}, t) = \mathbf{u}_{\pm}, \ t > 0 \text{ and } \mathbf{x}(\mathbf{X}, 0) = \mathbf{X},$$
 (2.9)

where u_+ are velocities fields for cations and anions. By mass conservation, the ionic densities satisfy the kinematic equations

$$\frac{\partial \rho_{\pm}}{\partial t} + \nabla \cdot (\rho_{\pm} u_{\pm}) = 0. \tag{2.10}$$

Alternatively, the kinematic mass conservation equations in the Lagrangian coordinate read [46]

$$\rho_{\pm}\left(\mathbf{x}_{\pm}(\mathbf{X},t),t\right) = \frac{\rho_{\pm}(\mathbf{X},0)}{\det\mathcal{F}},\tag{2.11}$$

where $\mathcal{F}(X,t)=\frac{\partial x(X,t)}{\partial X}$ is the deformation gradient tensor. The Least Action Principle states that the variation of the action functional with respect to the flow map gives the conservative force $F_{con,\pm} = \frac{\delta A(x_+(X,t),x_-(X,t))}{\delta x_\pm}$, where the action functional is defined as

$$\begin{split} A\left(\mathbf{x}_{+}(\boldsymbol{X},t),\mathbf{x}_{-}(\boldsymbol{X},t)\right) &= -\int_{0}^{t^{*}} F_{pot}(\Omega,t) + F_{ent}(\Omega,t) dt \\ &= A_{pot}\left(\mathbf{x}_{+}(\boldsymbol{X},t),\mathbf{x}_{-}(\boldsymbol{X},t)\right) + A_{ent}\left(\mathbf{x}_{+}(\boldsymbol{X},t),\mathbf{x}_{-}(\boldsymbol{X},t)\right) \end{split}$$

for some time $t^* > 0$. Here the kinetic energy of particles is assumed to be negligible.

Taking the derivation of conservative forces for cations as an example, we obtain by taking variation of actions with respect to the flow map $\mathbf{x}_{\perp}(\mathbf{X},t)$:

$$F_{con,+}^{ent} = \frac{\delta A_{ent} \left(\mathbf{x}_{+}(\mathbf{X}, t), \mathbf{x}_{-}(\mathbf{X}, t) \right)}{\delta \mathbf{x}_{+}(\mathbf{X}, t)}$$

$$= - \left[k_{B}T \nabla \rho_{+} + k_{B}T \frac{v \rho_{+}}{1 - \sum_{i=+} v \rho_{i}} \sum_{i=+} \nabla \rho_{i} + \frac{\partial P_{+}}{\partial T} \nabla T \right], \qquad (2.12)$$

where the thermal pressure for cations is given by

$$P_{+} = k_{B}T \left(\rho_{-} - \frac{1}{v}\right) \log \left(1 - \sum_{j=\pm} v \rho_{j}\right).$$

The mathematical details on the derivation of (2.12) are presented in the *Supporting Information*.

The conservative force due to the electrostatic potential energy can be analogously derived as follows [41,44]:

$$F_{con,+}^{pot} = \frac{\delta A_{pot} \left(\mathbf{x}_{+}(\mathbf{X}, t), \mathbf{x}_{-}(\mathbf{X}, t) \right)}{\delta \mathbf{x}_{+}}$$

$$= \frac{\delta}{\delta \mathbf{x}_{+}} \int_{0}^{t^{*}} -\left[\sum_{i,m=\pm} \frac{q_{i} q_{m}}{2} \iint_{\Omega_{i}^{x}} \rho_{i}(\mathbf{x}, t) \rho_{m}(\mathbf{x}', t) G(\mathbf{x}, \mathbf{x}') d\mathbf{x} d\mathbf{x}' \right]$$

$$+ \sum_{i=\pm} q_{i} \int_{\Omega_{i}^{x}} \rho_{i}(\mathbf{x}) \psi_{X}(\mathbf{x}, t) d\mathbf{x} d\mathbf{x}'$$

$$= -q_{+} \rho_{+} \nabla \phi, \qquad (2.13)$$

where $\phi(\mathbf{x},t) = \psi_X(\mathbf{x},t) + \sum_{i=\pm} q_i \int_{\Omega} \rho_i(\mathbf{x}',t) G(\mathbf{x},\mathbf{x}') d\mathbf{x}'$ is the electric potential. Combination of $F_{con,\pm}^{ent}$ and $F_{con,\pm}^{pot}$ leads to the conservative force for cations and anions:

$$F_{con,\pm} = -\left(k_B T \nabla \rho_{\pm} + k_B T \frac{v \rho_{\pm}}{1 - \sum_{i=\pm} v \rho_i} \sum_{j=\pm} \nabla \rho_j + q_{\pm} \rho_{\pm} \nabla \phi + \frac{\partial P_{\pm}}{\partial T} \nabla T\right). \tag{2.14}$$

In order to predict the irreversible heat generation, we consider entropy production functional $\Delta(V,t)=\int_V\widetilde{\Delta}(x,t)dx$ for an arbitrary domain V, with the entropy production density given by

$$\widetilde{\Delta} = \sum_{i=+} \frac{v_i \rho_i |u_i|^2}{T} + \frac{1}{k} \left| \frac{J_h}{T} \right|^2.$$
 (2.15)

Here v_i is the viscosity of ions of the ith species, j_h represents for the heat flux, and k is a constant related to the heat conductance. We employ the Maximum Dissipation Principle (MDP) to derive dissipative forces by taking variation of the dissipation functional Δ with respect to the rates (velocity) in Eulerian coordinates, i.e.,

$$\boldsymbol{F}_{dis,+}(\boldsymbol{x},t) = \frac{T}{2} \frac{\delta \Delta(\Omega,t)}{\delta \boldsymbol{u}_{-}(\boldsymbol{x},t)} = v_{+} \rho_{+} \boldsymbol{u}_{+}. \tag{2.16}$$

Note that the factor $\frac{1}{2}$ is included due to the convention that the energy dissipation is always a quadratic function of certain rates.

Therefore, the balance of conservative forces and dissipative forces yields

$$\begin{split} &v_{\pm}\rho_{\pm}\boldsymbol{u}_{\pm}\\ &=-\left(k_{B}T\nabla\rho_{\pm}+\frac{\partial P_{\pm}}{\partial T}\nabla T+k_{B}T\frac{\upsilon\rho_{\pm}}{1-\sum_{i=\pm}\upsilon\rho_{i}}\sum_{j=\pm}\nabla\rho_{j}+q_{\pm}\rho_{\pm}\nabla\phi\right). \end{split} \tag{2.17}$$

Combining the mass conservation equation (2.10), one obtains modified Nernst–Planck (NP) equations that include ionic steric effect and thermal effect for ion transport:

$$\begin{split} &\frac{\partial \rho_{\pm}}{\partial t} \\ &= \frac{1}{\nu_{\pm}} \nabla \cdot \left(k_B T \nabla \rho_{\pm} + \frac{\partial P_{\pm}}{\partial T} \nabla T + k_B T \frac{\nu \rho_{\pm}}{1 - \sum_{i = \pm} \nu \rho_i} \sum_{j = \pm} \nabla \rho_j + q_{\pm} \rho_{\pm} \nabla \phi \right). \end{split} \tag{2.18}$$

Note that the second term in the right side of the modified NP equation (2.18) can be regarded as the Soret effect that describes ion motion due to temperature gradient [47,48]. In addition, it is remarked that for an isothermal case, the modified NP Eqs. (2.18) reduces to the modified NP equations with ionic steric effects in the work [43].

With (2.17), we define the ionic flux density by $j_{\pm}=\rho_{\pm}u_{\pm}$. Since the electrodes are two blocking walls without electrochemical reaction, zero-flux boundary conditions are imposed at the Stern/diffuse layer interface at x=-L and x=L, i.e.,

$$j_{+}(-L,t) = 0$$
 and $j_{+}(L,t) = 0$. (2.19)

2.2. Poisson's equation

The electric potential $\phi(x, t)$ is determined by the Poisson's equation

$$-\nabla \cdot \epsilon_0 \epsilon_r \nabla \phi(\mathbf{x}, t) = \sum_{i=+} q_i \rho_i(\mathbf{x}, t). \tag{2.20}$$

To take the Stern layers of width H into account, we impose Robin boundary conditions for the electric potential at x = -L and x = L as shown in Fig. 1:

$$\phi(\pm L, t) \pm H \frac{\partial \phi}{\partial x}(\pm L, t) = \mp \phi_s(t), \tag{2.21}$$

where ϕ_s is the applied potential at the electrode surface. In Cyclic Voltammetry (CV) measurements, $\phi_s(t)$ is prescribed periodically and linearly with time as [49]

$$\phi_s(t) = \begin{cases} \phi_{min} + vt, & 2(n-1)t_0 \le t < (2n-1)t_0, \\ \phi_{max} - v \left[t - (2n-1)t_0 \right], & (2n-1)t_0 \le t < 2nt_0, \end{cases}$$
 where v is the scan rate in V/s and $n = 1, 2, 3, ...$ is the number of

where ν is the scan rate in V/s and n(=1,2,3,...) is the number of cycles. In such CV measurements, $\tau_{cv} = (\phi_{max} - \phi_{min})/\nu$ denotes the half cycle period.

2.3. Energy conservation equation

The first law of thermodynamics that describes energy conservation is employed here to derive the governing equation for temperature evolution. Consider an arbitrary control volume V that does not move along with the flow maps of ions. The rate of work done on V is given by

$$\begin{split} \frac{d}{dt}W(V,t) &= \sum_{i=\pm} q_i \int_V \rho_i \frac{\partial}{\partial t} \left[\psi_X(\mathbf{x},t) + \sum_{m=\pm} q_m \int_{\Omega \setminus V} \rho_m(\mathbf{x}') G(\mathbf{x},\mathbf{x}') d\mathbf{x}' \right] d\mathbf{x} \\ &+ \sum_{i=\pm} \int_{\partial V} -P_i(\mathbf{x},t) \mathbf{u}_i(\mathbf{x},t) \cdot d\mathbf{S}, \end{split}$$

(2.23)

where the first term represents the rate of work done by a time-dependent electric potential outside V, including the contributions from ions in the domain $\Omega \backslash V$ and external potential ψ_X . The second term describes the rate of work done by the thermal pressure P_i through the boundary of V. The rate of heat transfer is given by the heat flux J_h through ∂V :

$$\frac{d}{dt}Q(V,t) = -\int_{\partial V} \mathbf{j}_h \cdot d\mathbf{S}.$$
 (2.24)

Since V does not move with the flow maps of ions, we need to consider the total energy flux J_E through the boundary:

$$J_{E}(V,t) = \sum_{i=+} \int_{\partial V} \left(q_{i} \rho_{i} \phi + e_{i}^{int} \right) \mathbf{u}_{i} \cdot dS, \tag{2.25}$$

where $e_i^{int}=\Psi_i-T\frac{\partial\Psi_i}{\partial T}$ is the internal energy density, with Ψ_i defined in (2.5). Note that $e_\pm^{int}=0$ due to the linearity of Ψ_\pm with respect to T. By the arbitrariness of the control volume V, we derive from the energy conservation

$$\frac{d}{dt}U(V,t) + J_E(V,t) = \frac{d}{dt}W(V,t) + \frac{d}{dt}Q(V,t), \tag{2.26}$$

(2.7), and (2.23)-(2.25) that

$$\frac{k_B C_0}{v} \frac{\partial T}{\partial t} = \nabla \cdot (k \nabla T) - \sum_{i=+} \nabla \cdot (P_i \mathbf{u}_i) - \sum_{i=+} q_i \rho_i \mathbf{u}_i \cdot \nabla \phi. \tag{2.27}$$

Here the first term in the right describes heat diffusion, the second term represents the work of thermal pressure converted into heat, and the third term that includes irreversible Joule heating describes the heat converted from electrostatic interactions. The derivation details for (2.27) can be found in *Supporting Information*.

To describe thermally insulated electrodes, the boundary conditions of the temperature equation (2.27) are prescribed by

$$\frac{\partial T}{\partial x}(\pm L) = 0. {(2.28)}$$

2.4. Governing equations

In summary, we have the following governing equations to describe the thermal electrokinetics of EDLCs:

$$\begin{cases} -\nabla \cdot \varepsilon_0 \varepsilon_r \nabla \phi = \sum_{i=\pm} q_i \rho_i, \\ \frac{\partial \rho_\pm}{\partial t} + \nabla \cdot \left(\rho_\pm \mathbf{u}_\pm \right) = 0, \\ \rho_\pm \mathbf{u}_\pm = -\frac{1}{\nu_\pm} \left(k_B T \nabla \rho_\pm + \frac{\partial P_\pm}{\partial T} \nabla T + k_B T \frac{\upsilon \rho_\pm}{1 - \sum_{i=\pm} \upsilon \rho_i} \sum_{j=\pm} \nabla \rho_j + q_\pm \rho_\pm \nabla \phi \right), \\ \frac{k_B C_0}{\upsilon} \frac{\partial T}{\partial t} = \nabla \cdot (k \nabla T) - \sum_{i=\pm} \nabla \cdot (P_i \mathbf{u}_i) - \sum_{i=\pm} q_i \rho_i \mathbf{u}_i \cdot \nabla \phi, \\ P_\pm = k_B T \left(\rho_\mp - \frac{1}{\upsilon} \right) \log \left(1 - \sum_{j=\pm} \upsilon \rho_j \right). \end{cases}$$

To nondimensionalize the equations, we introduce reference temperature T_0 , microscopic length scale $\lambda_D = \sqrt{\frac{\epsilon_0 \epsilon_r k_B T_0}{2e^2 \rho_\infty}}$, density ρ_∞ , viscosity ν_0 , and time scale $\tau = \frac{\lambda_D L \nu_0}{k_B T_0}$. Also, we introduce dimensionless quantities $\widetilde{x} = x/L$, $\widetilde{t} = t/\tau$, $\widetilde{T} = T/T_0$, $\widetilde{v} = 2v\rho_\infty$, $\widetilde{\phi} = \frac{e\phi}{k_B T_0}$, $\widetilde{k} = \frac{\tau k}{2k_B \rho_\infty L^2}$, and $\epsilon = \lambda_D/L$, which is often a small parameter for macroscopic EDLCs. For binary monovalent electrolyte solutions under consideration, we assume $\nu_\pm = \nu_0$, consider salt density $\widetilde{c} = \frac{\rho_+ + \rho_-}{2\rho_\infty}$ and charge density $\widetilde{\rho} = \frac{\rho_+ - \rho_-}{2\rho_\infty}$, and introduce $s = \log(1 - \widetilde{v}\widetilde{c})$. Dropping the tildes in new variables, we have

$$\begin{cases} \frac{\partial c}{\partial t} = -\epsilon \frac{\partial j_c}{\partial x}, & j_c = -\left(\frac{T}{1 - vc} \frac{\partial c}{\partial x} + \rho \frac{\partial \phi}{\partial x} - \frac{2 - vc}{v} s \frac{\partial T}{\partial x}\right), \\ \frac{\partial \rho}{\partial t} = -\epsilon \frac{\partial j_\rho}{\partial x}, & j_\rho = -\left(T \frac{\partial \rho}{\partial x} + c \frac{\partial \phi}{\partial x} + T \frac{v\rho}{1 - vc} \frac{\partial c}{\partial x} - \rho s \frac{\partial T}{\partial x}\right), \end{cases}$$
(2.30)

where j_{ρ} is the dimensionless Faradaic current scaled by $j_0=2e\rho_{\infty}v/Lk_BT_0$, and j_c is the dimensionless salt current. Thus, we have the following relations between the reduced variables and original density and velocity of each ionic species:

$$\rho_{\pm} = c \pm \rho, \quad u_{\pm} = \frac{j_c \pm j_{\rho}}{c \pm \rho}. \tag{2.31}$$

Finally, we have the following reformulated dimensionless governing equations for the electric potential, densities, and temperature:

$$\begin{cases} -\epsilon^{2} \frac{\partial^{2} \phi}{\partial x^{2}} = \rho, \\ \frac{\partial c}{\partial t} = -\epsilon \frac{\partial j_{c}}{\partial x}, \quad j_{c} = -\left(\frac{T}{1 - vc} \frac{\partial c}{\partial x} + \rho \frac{\partial \phi}{\partial x} - \frac{2 - vc}{v} s \frac{\partial T}{\partial x}\right), \\ \frac{\partial \rho}{\partial t} = -\epsilon \frac{\partial j_{\rho}}{\partial x}, \quad j_{\rho} = -\left(T \frac{\partial \rho}{\partial x} + c \frac{\partial \phi}{\partial x} + T \frac{v\rho}{1 - vc} \frac{\partial c}{\partial x} - \rho s \frac{\partial T}{\partial x}\right), \\ \frac{C_{0}}{v} \frac{\partial T}{\partial t} = k \frac{\partial^{2} T}{\partial x^{2}} - \epsilon \sum_{i = \pm} \frac{\partial}{\partial x} (P_{i} u_{i}) - \epsilon j_{\rho} \frac{\partial \phi}{\partial x}, \end{cases}$$

$$(2.32)$$

where
$$s = \log(1 - vc)$$
 and $P_{\pm} = \frac{v\rho_{\mp} - 1}{v} T \log(1 - \sum_{j=\pm} v\rho_j)$.

2.5. Numerical method

The system (2.32) with boundary conditions (2.19), (2.21), and (2.28) is a numerically challenging problem, especially when boundary layers present due to small ϵ for macroscopic EDLCs. For temporal integration, we propose a fully implicit time-discretization scheme

$$\begin{cases} -e^{2} \frac{\partial^{2} \phi^{n+1}}{\partial x^{2}} = \rho^{n+1}, \\ \frac{c^{n+1} - c^{n}}{\Delta t} = -e^{2} \frac{\partial j_{c}^{n+1}}{\partial x}, \\ j_{c}^{n+1} = -\left(\frac{T^{n+1}}{1 - vc^{n+1}} \frac{\partial c^{n+1}}{\partial x} + \rho^{n+1} \frac{\partial \phi^{n+1}}{\partial x} - \frac{2 - vc^{n+1}}{v} s^{n+1} \frac{\partial T^{n+1}}{\partial x}\right), \\ \frac{\rho^{n+1} - \rho^{n}}{\Delta t} = -e^{2} \frac{\partial j_{\rho}^{n+1}}{\partial x}, \\ j_{\rho}^{n+1} = -\left(T^{n+1} \frac{\partial \rho^{n+1}}{\partial x} + c^{n+1} \frac{\partial \phi^{n+1}}{\partial x} + c^{n+1} \frac{\partial T^{n+1}}{\partial x}\right), \\ +T^{n+1} \frac{v\rho^{n+1}}{1 - vc^{n+1}} \frac{\partial c^{n+1}}{\partial x} - \rho^{n+1} s^{n+1} \frac{\partial T^{n+1}}{\partial x}\right), \\ \frac{C_{0}}{v} \frac{T^{n+1} - T^{n}}{\Delta t} = k \frac{\partial^{2} T^{n+1}}{\partial x^{2}} - e^{2} \frac{\partial}{\partial x} \left(P_{+}^{n+1} u_{+}^{n+1} + P_{-}^{n+1} u_{-}^{n+1}\right) - e^{2} j_{\rho}^{n+1} \frac{\partial \phi^{n+1}}{\partial x}, \end{cases}$$

$$(2.33)$$

where Δt is a time step size, and c^n , ρ^n , T^n , and ϕ^n are numerical approximations of $c(\cdot,t_n)$, $\rho(\cdot,t_n)$, $T(\cdot,t_n)$, and $\phi(\cdot,t_n)$ at $t_n=n\Delta t$, respectively.

After temporal discretization, the system (2.33) with boundary conditions is spatially discretized with a collocation method implemented in BVP4C [50] in the Matlab. For small ϵ , boundary layers are resolved with an adaptive, nonuniform mesh, in which grid points are densely distributed adjacent to the electrodes. The resulting nonlinear algebraic equations are solved iteratively by Newton-type methods. A strategy of continuation on the parameter ϵ is adopted to generate good initial guesses for iterations at the first time step. Further numerical details are presented in the *Supporting Information*.

3. Results

To demonstrate the performance of the proposed model, extensive numerical simulations based on the model are conducted to investigate the effect of charging-discharging scan rates and ionic sizes on the thermal electrokinetics of EDLCs and unravel underlying mechanism of the reversible and irreversible heat generation. In the periodic chargingdischarging processes, a time-dependent voltage is applied through the boundary condition (2.21) with the scheme (2.22), in which the maximum and minimum surface electric potentials are set as $\psi_{max}=1~\mathrm{V}$ and $\psi_{min} = 0$ V. We consider monovalent binary electrolyte solutions that are blocked by two thermally insulated electrodes. Unless specified otherwise, the electrolyte relative permittivity is taken as that of water $\epsilon_r = 66.1$, uniform ionic diffusion coefficients $D_{\pm} = k_B T_0 / v_{\pm} =$ 1.7×10^{-10} m²/s are considered, and typical solvated ion diameter a is used, ranging from 0.50 to 0.68 nm [24]. The initial and bulk ion concentrations are set as $\rho_{\infty} = 1M$, which gives $\lambda_D = 0.3$ nm. To simulate macroscopic EDLCs, we consider a computational domain [-L, L] with L = 1 µm. Therefore, $\epsilon = 0.0003$ which indicates that there are thin boundary layers closed to electrodes.

3.1. Charging dynamics

The proposed model is first applied to study thermal electrokinetics of an EDLC charging to steady states. A fixed surface potential $\phi_s(t) \equiv 20 \left(k_B T_0/e\right)$ is applied at electrodes; cf. the Robin boundary conditions (2.21). The simulations take a uniform ionic size a=

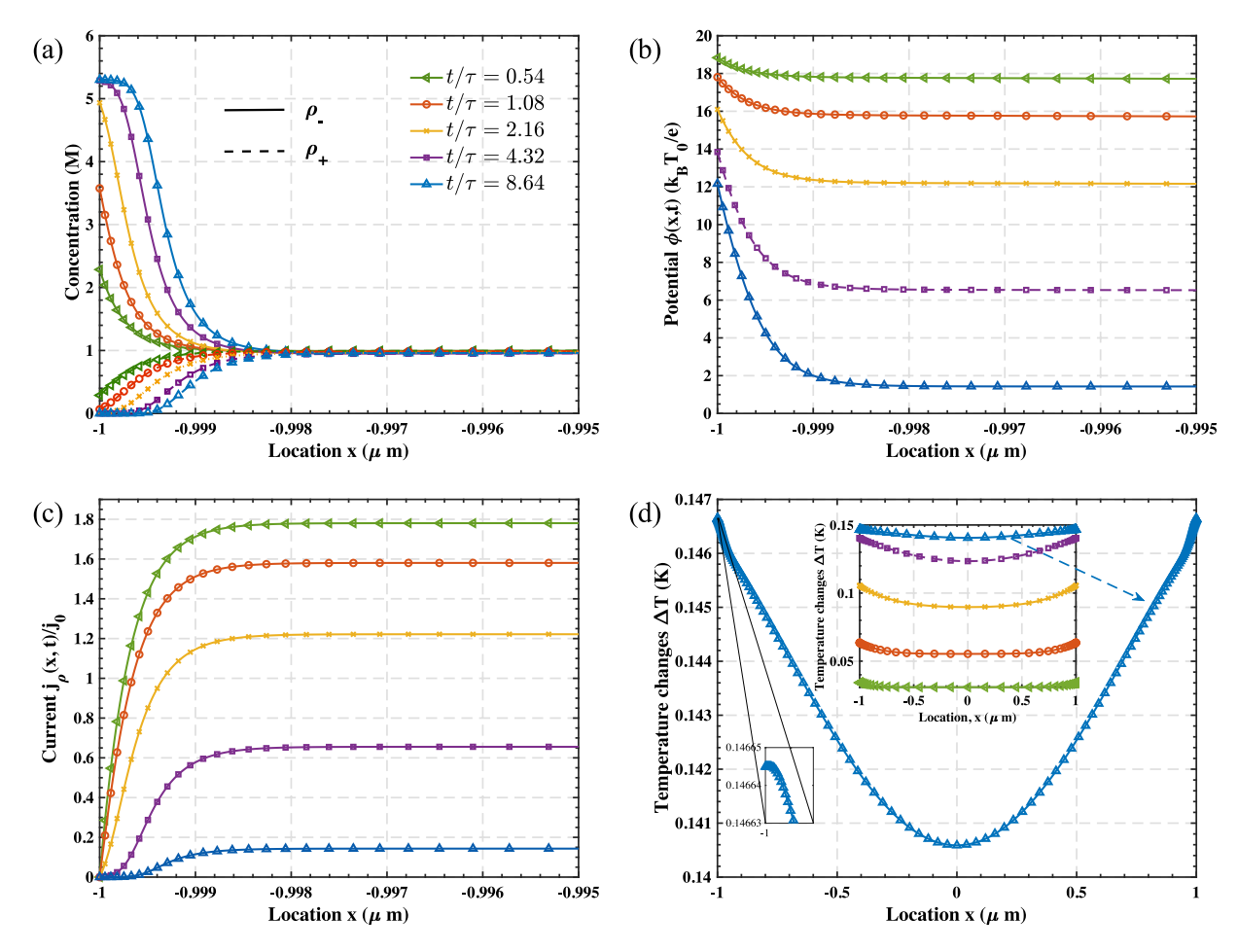


Fig. 2. Snapshots of ionic concentration $\rho_+(\mathbf{x},t)$ profiles (a), electric potential $\phi(\mathbf{x},t)$ profiles (b), current density $j_{\varrho}(\mathbf{x},t)$ profiles (c), and temperature $T(\mathbf{x},t)$ profiles (d).

0.68 nm, which implies a saturation concentration $\rho_{max}=1/a^3=5.3M$. As displayed in Fig. 2(a), counterions gradually accumulate next to the surface with the applied voltage, and the concentration eventually reaches a saturation concentration due to steric hindrance. By contrast, coions are depleted away from the electrode due to the electrostatic interaction. As the charging process reaches a steady state, a pronounced saturated layer with uniform concentration $\rho_-=\rho_{max}$ forms near electrodes. Fig. 2(b) depicts the profiles of electrostatic potential as charging process proceeds. Notice that the potential first drops linearly from the surface value ϕ_s within the Stern layer H. In addition, the electrostatic potential further gets screened quickly because of the attracted counterions in the EDL.

Fig. 2(c) shows the current density distribution $j_o(\mathbf{x},t)$ (rescaled by j_0) during the charging process. Since zero-flux boundary conditions are imposed, the current density vanishes in the Stern layer for the entire charging process. In initial stages, there is large current density extending into bulk regions, ascribing to the transport of the attracted of counterions and repulsed of coions. As the saturation layer builds up, the electrostatic interactions get screened and the current both in EDL and bulk decreases. Eventually, the current vanishes everywhere when the system approaches the steady state. Overall, it should be emphasized that ionic concentrations, potential, and current all level off quickly to bulk values within a very thin boundary layer next to the electrode (about $0.002\mu m$ width). The inset of Fig. 2(d) shows that the profiles of temperature T(x, t) exhibit a parabolic shape for the whole domain during the charging process. The temperature at boundaries takes the lead to rise in that the heat source terms contribute significantly more than that in the bulk. This is further confirmed in the analysis of heat generation presented in Section 3.3. The internal

bulk electrolytes subsequently get heated up as well, due to the heat diffusion and heat generation in the bulk. We note that the bulk region also contributes a fair amount of heat in the system, because its size is much larger than the boundary layers. With thermally insulated boundary conditions, the temperature becomes homogeneous everywhere in the steady state. To better understand the spatial distribution of temperature at certain time, the main plot of Fig. 2(d) delineates the profile of temperature T(x,t) at $t/\tau = 8.64$. In addition to an overall parabolic shape, mild kinks emerge at the interfaces between the boundary layers and the bulk. Such kinks can be explained by the analysis on heat generation source terms; cf. Section 3.3.

3.2. Periodic charging and discharging

The proposed model is also applied to probe thermal electrokinetics in EDLCs with a linearly varying surface potential ϕ_s given by (2.22), in which $\phi_{min}=0(k_BT_0/e)$ and $\phi_{max}=20(k_BT_0/e)$; cf. the inset plot of Fig. 3(a). Various ionic sizes and cyclic voltammetry scan rates are considered to evaluate their impact on the thermal electrokinetics. Fig. 3(a), the counterion concentration at the Stern/diffuse layer interface increases synchronously as the potential rises, and reaches their maximum allowable saturation values that are determined by their ionic sizes. As the potential decreases, the concentration declines synchronously back to the initial bulk values at the end of cycles. Fig. 3(b) presents the periodic evolution of current density in the bulk region. Obviously, one can observe that the current surges drastically to a maximum value, and then decreases gradually, in that electrostatic attractions, i.e., the driving force, are weakened by the accumulated ions. Comparing two current curves, one can see that the smaller ionic

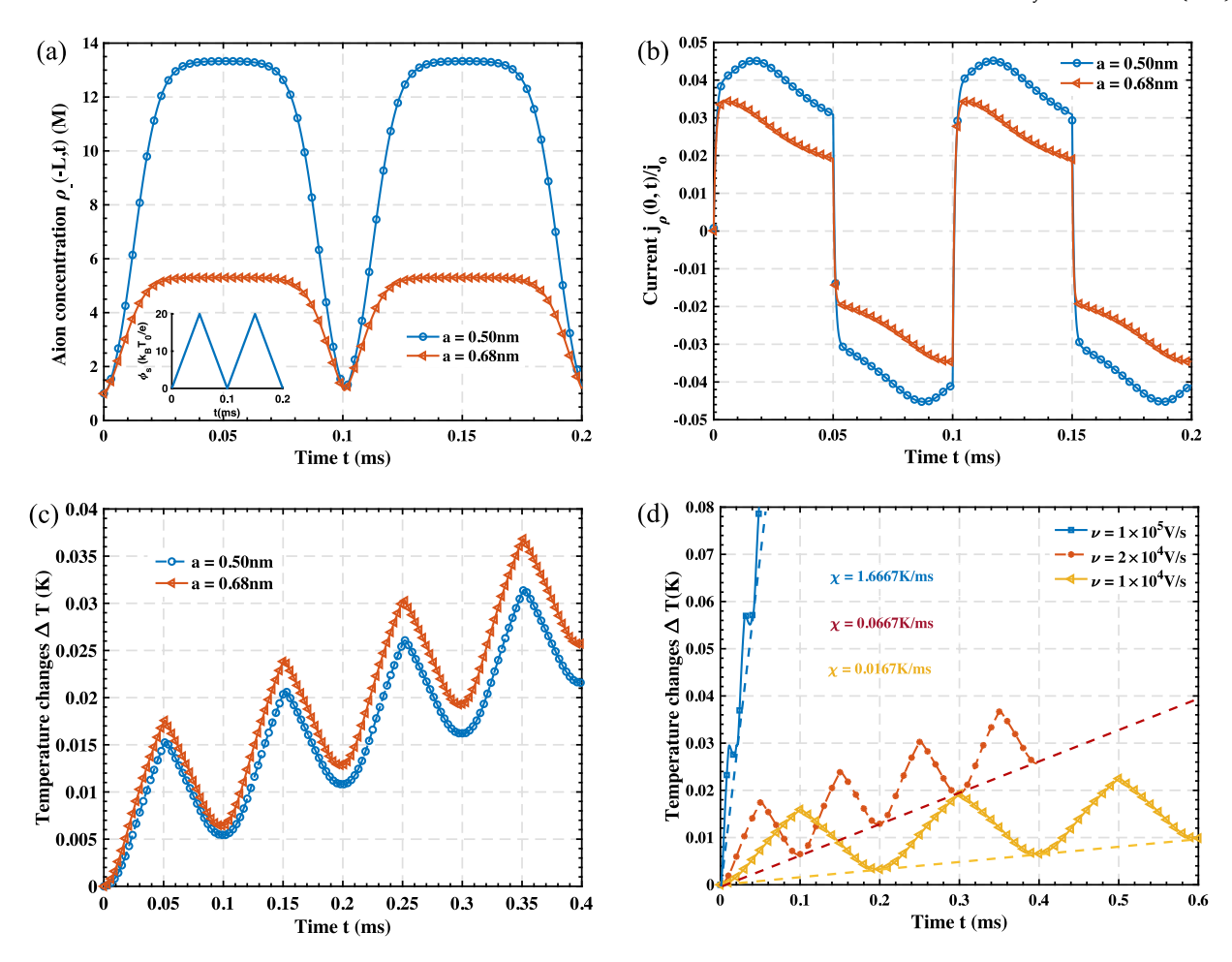


Fig. 3. Evolution of counterion concentration $\rho_-(-L,t)$ (a), current density $j_\rho(0,t)$ in the bulk (b), and temperature change $\Delta T = T(-L,t) - T(-L,0)$ (c), using the cyclic voltammetry scan rate $\nu = 2 \times 10^4 V/s$ and different ionic diameters a = 0.50 nm and a = 0.68 nm. (d) Temperature change ΔT at electrodes using different scan rate ν and an ionic diameter a = 0.68 nm. The parameter χ denotes the slope of dash lines that reflect the linear increase of ΔT with respect to time.

size has larger maximum flux, since more ions are allowed to transport into EDLs. After $t=0.05\,$ ms, the potential begins to decrease linearly and the attracted ions in the EDL start to diffuse back to the bulk. This explains the abrupt switching of the positive charge current to negative charge current at the same time. In addition, the shape of the profile before and after $t=0.05\,$ ms is highly symmetric.

In addition, simulations are performed to assess the impact of ionic size on the temperature in continuous charging-discharging cycles. From Fig. 3(c), one can see that the temperature at the Stern/diffuse layer interface rises in a sawtooth shape. It is heated up monotonically in a charging stage, and partially cooled down in a discharging stage. This demonstrates that the proposed model is able to capture the reversible and irreversible heat generation in the charging-discharging cycles. Overall, the temperature still rises oscillatory due to the irreversible contribution. Furthermore, it is seen that a larger ionic diameter a contributes more irreversible heat, leading to overall steeper temperature rise. To further quantify the temperature rise, we use χ to denote the slope of overall temperature rise; cf. Fig. 3(d). This figure presents the effect of scan rate of ϕ_s on the temperature rise. It is found that, when the scan rate changes from $v = 1 \times 10^4 \text{ V/s}$ to $v = 2 \times 10^4 \text{ V/s}$, the slope χ is correspondingly magnified by four times. Further increase from $v = 2 \times 10^4$ V/s to $v = 1 \times 10^5$ V/s reveals the scaling relation $\chi \propto v^2$.

To further quantitatively study the scaling relation of χ against a and v, we perform additional simulations with a larger range of a and v. It is of interest to observe from Fig. 4 that the slope of temperature rise χ depends linearly on the ionic diameter a, showing that more irreversible heat is generated in each charging/discharging period with

a larger ionic diameter. In addition, the log-log plot of χ against v^2 shows a perfect scaling relation $\chi \propto v^2$. To understand this, we define the average current \bar{I} of a voltammetry cycle as

$$\bar{I} = \frac{\int_{t=0}^{\tau_{cv}} j_{\rho}(0,t)dt}{\tau_{cv}},$$
(3.1)

where τ_{cv} is the half cycle period. Numerical results find that the average current \bar{I} scales linearly with the increase of v. Therefore, it comes to the conclusion that the contribution of irreversible heat, represented by χ , is proportional to the square of the current, i.e., $\chi \propto \bar{I}^2$. Such a conclusion is consistent with previous understanding on Joule heating effect [17,22,23].

3.3. Heat generation

To further understand the heat generation of the proposed model, we investigate contributions of two source terms of the temperature evolution equation in (2.32): $-j_{\rho} \cdot \nabla \phi$ due to the charge current and $-\sum_{i=\pm} \nabla \cdot (P_i u_i)$ due to the thermal pressure. Fig. 5(a) and (b) compare such two terms in the charging and discharging stage. First, both terms are positive in the charging stage and negative in the discharging stage, indicating that they are both exothermic and endothermic in charging and discharging stages, respectively. In addition, the contribution made by the term due to charge current is a bit more significant than the term due to thermal pressure in the whole charging–discharging cycle. It is interesting to note that such terms both vanish at the boundary, and mainly concentrate and peak in the boundary layers. Although such terms are small in the bulk region, the bulk region is much larger than

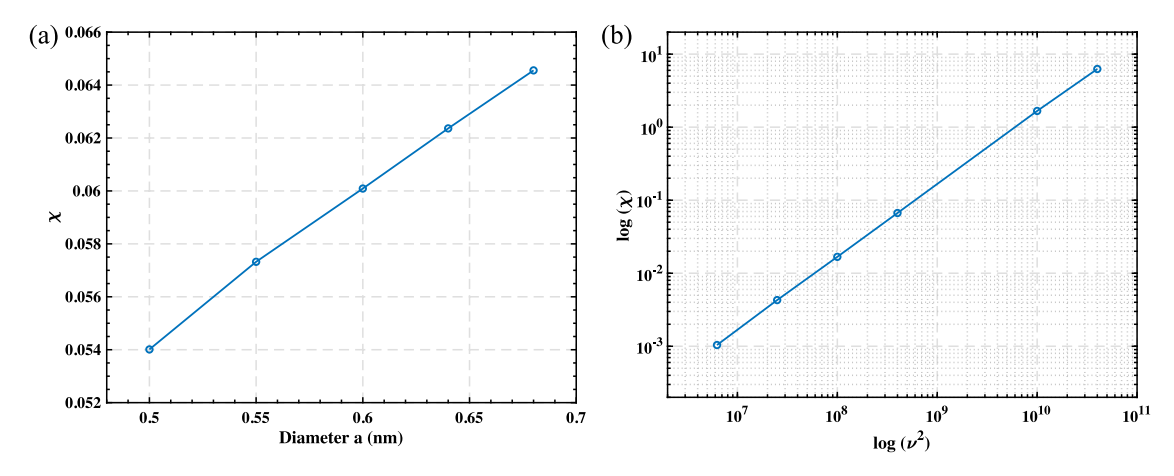


Fig. 4. (a) A plot of χ against the ionic diameter a; (b) A log-log plot of χ against v^2 .

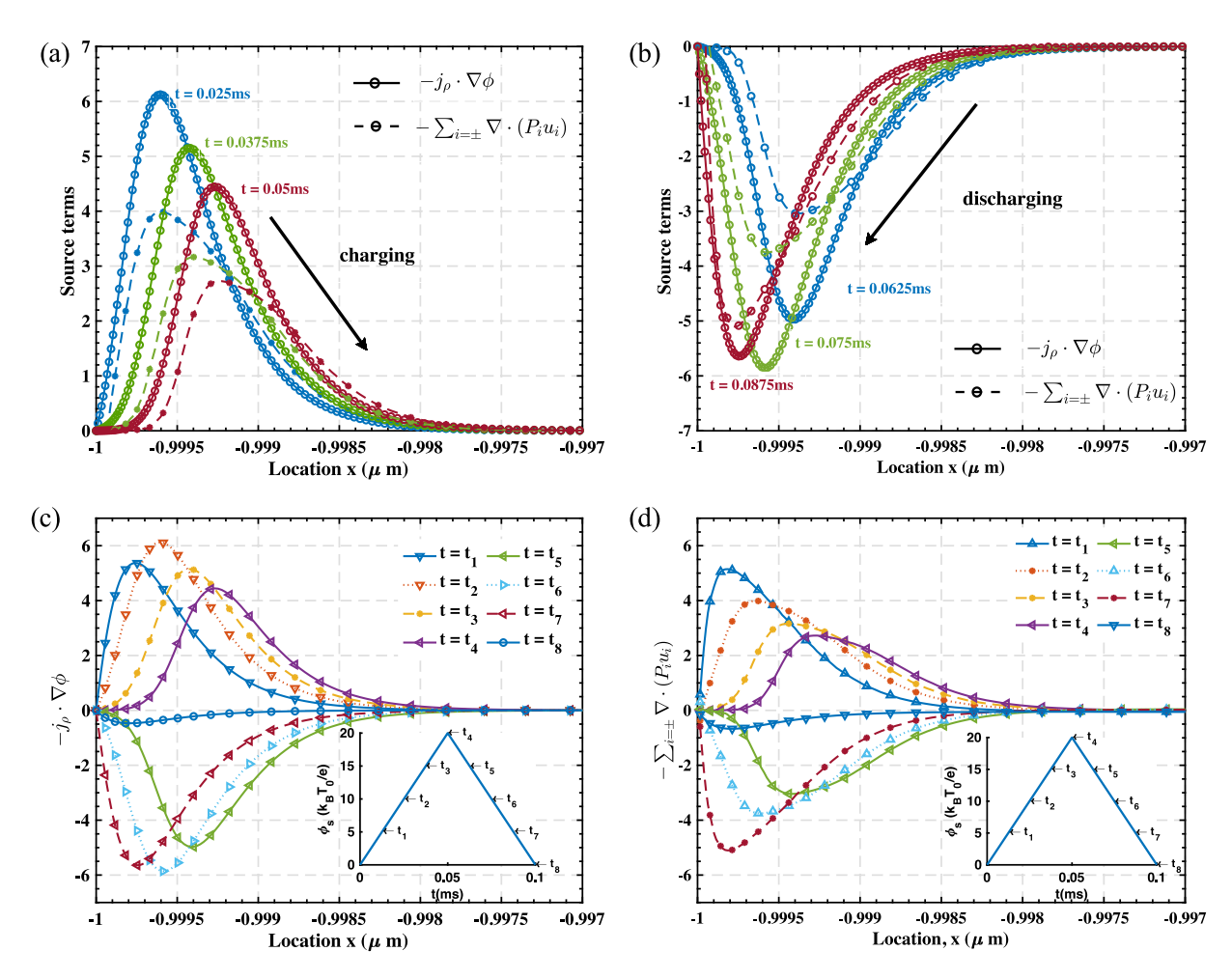


Fig. 5. Comparison of two heat generation source terms in the charging (a) and discharging (b) stage. Evolution of the source terms $-j_{\rho} \cdot \nabla \phi$ (c) and $-\sum_{i=\pm} \nabla \cdot (P_{i}u_{i})$ (d) in one charging–discharging cycle.

the boundary layers and therefore they still contribute a fair amount of heat in charging–discharging cycles.

In order to understand the dynamics of such terms, we also plot the distribution of such terms in various phases in one charging-discharging cycle. Fig. 5(c) and (d) display 8 snapshots of the distribution of the terms at times that divide the cycle into 8 phases; cf. the labels in the inset. The source term due to charge current rises positively and reaches the maximum value at the first quarter of the cycle. After that, the profile lowers with the position of the peaks

moving away from the electrode, and suddenly changes its sign in the second half of the cycle. For the second half, i.e., the discharging process, the profile follows a similar pattern, rising negatively in the third quarter and diminishing in the fourth quarter. For the term due to thermal pressure, the profiles in Fig. 5(d) show a different pattern—it reaches the maximum in the first quarter, then damps in the rest of charging process, and keeps rising negatively in discharging process until the seven eighths of one cycle. Notice that the peaks of both terms move away from the electrode in the charging process

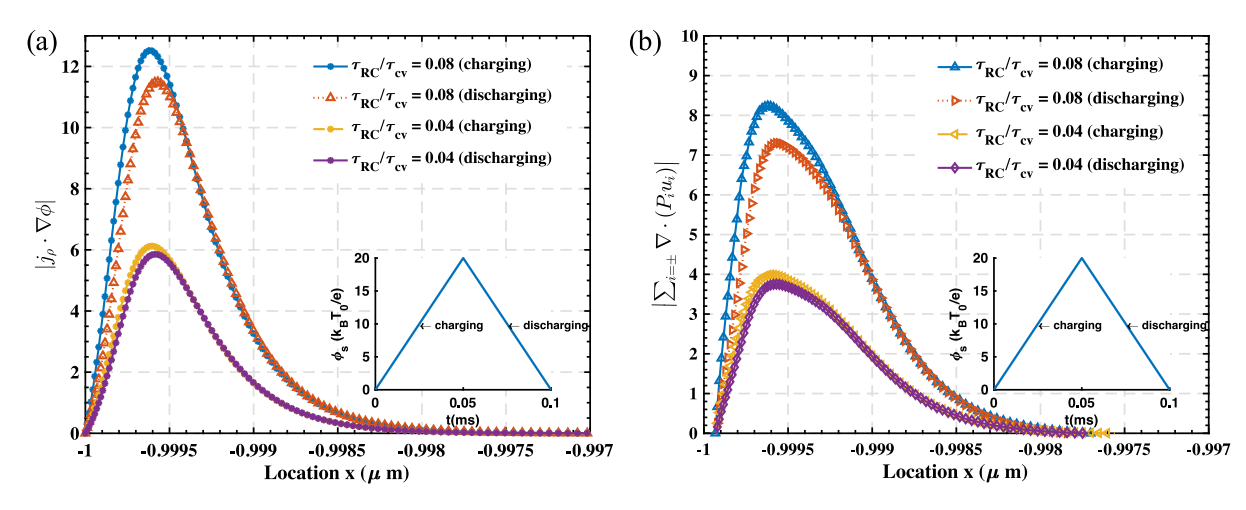


Fig. 6. The magnitude of heat generation source terms $j_{\rho} \cdot \nabla \phi$ (a) and $\sum_{i=\pm} \nabla \cdot (P_i u_i)$ (b) with different scan rates of surface potential in the middle of charging and discharging stages.

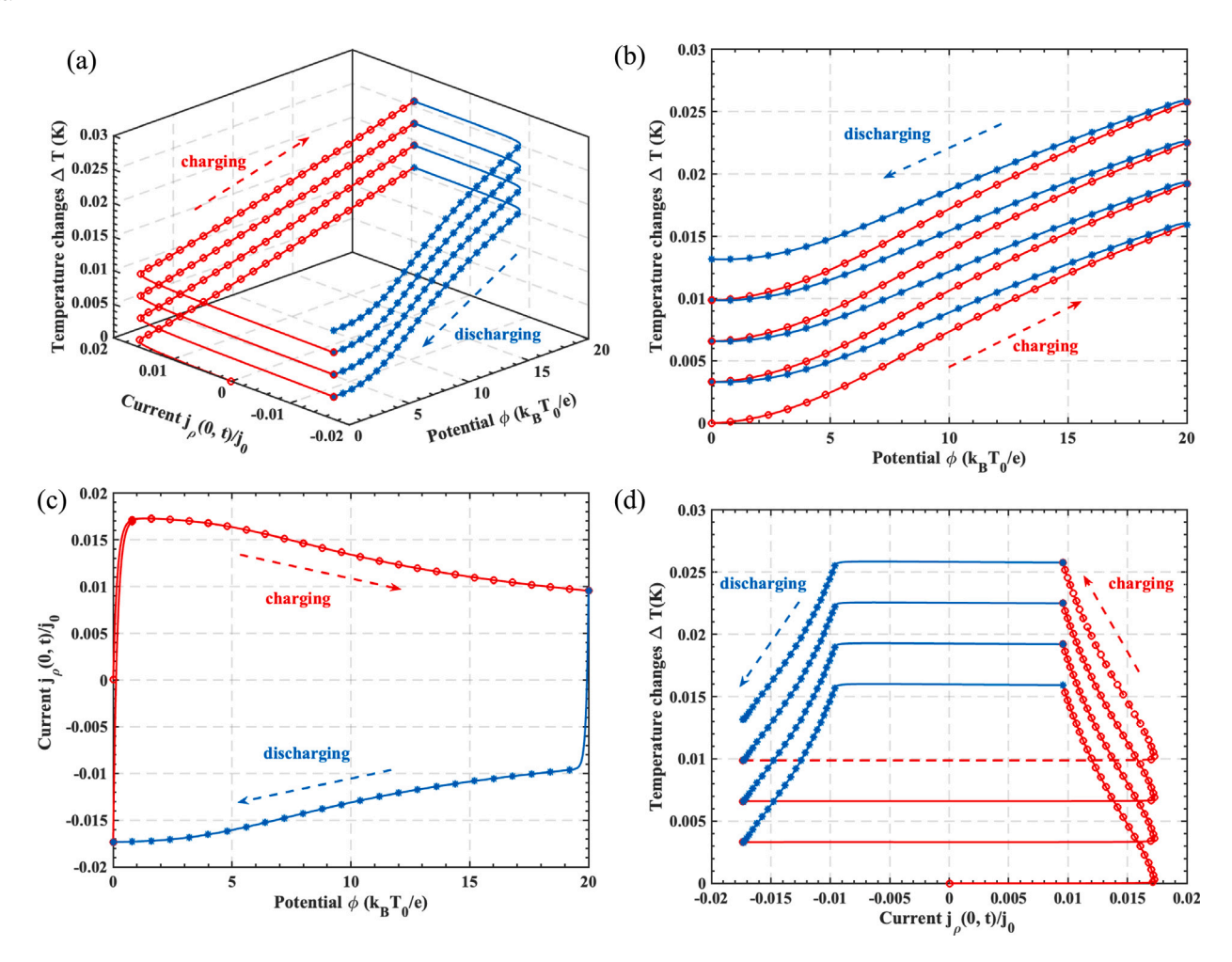


Fig. 7. (a) Evolution curve of the charge current in the bulk $j_{\rho}(0,t)$, the electrostatic surface potential $\phi_s(t)$, and the temperature change ΔT compared to the initial temperature at electrodes in cyclic voltammetry measurements; (b) Projection of the evolution curve to the $\phi_s - \Delta T$ plane; (c) Projection of the evolution curve to the $\phi_s - j_{\rho}$ plane; (d) Projection of the evolution curve to the $j_{\rho} - \Delta T$ plane. The red ring symbols represent the charging process, and the blue star symbols represent the discharging process. (For interpretation of the references to color in this figure legend, the reader is referred to the web version of this article.)

and approach the electrode in the discharging process. This can be explained by the fact that the accumulated counterions are piling up in layers at electrodes due to steric hindrance in the charging process, and the layering counterions dissolve back to the bulk in the discharging process.

To understand the impact of scan rate on the heat generation, simulations are also performed with different scan rates that are represented by $\tau_{cv}=\frac{\psi_{max}-\psi_{min}}{\nu}.$ It has been systematically studied that the dimensionless ratio τ_{RC}/τ_{cv} is a key parameter to characterize the CV measurements [32,51]. Here $\tau_{RC}=\frac{\lambda_DL\nu_0}{k_BT_0}$ is the characteristic

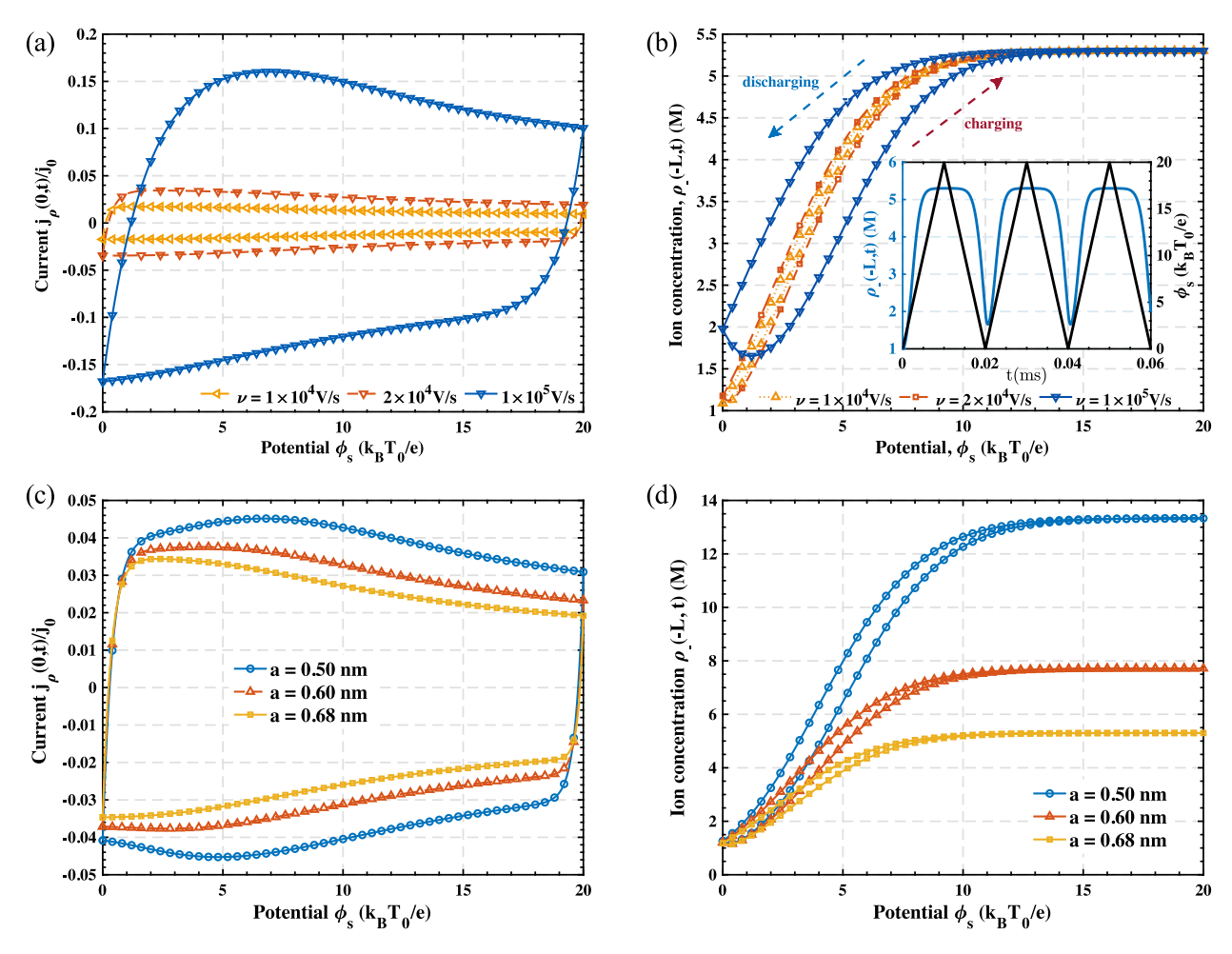


Fig. 8. The $j_{\rho} - \phi_s$ curve (a) and $\rho_-(-L,t) - \phi_s$ curve (b) in CV simulations with various scan rates in one cycle. The inset plot gives the surface potential and counterion concentration against time. The $j_{\rho} - \phi_s$ curve (c) and $\rho_-(-L,t) - \phi_s$ curve (d) in CV simulations with various ionic sizes in one cycle.

relaxation timescale. As shown in Fig. 6 (a), the difference of the magnitude of $j_{\rho} \cdot \nabla \phi$ in the charging and discharging stages is magnified as the timescale ratio increases. Similar results can be observed for the heat source term $|\sum_{i=\pm} \nabla \cdot (P_i u_i)|$. The difference of the magnitude in charging and discharging processes is related to the irreversible heat generation in EDLCs. Such results are consistent with the results shown in Fig. 3(d) that temperature rise over cycles due to irreversible heat generation is enhanced significantly as the scan rate increases.

3.4. Cyclic voltammetry

Cyclic voltammetry is a very powerful method to characterize the performance of electrochemical devices under various conditions [27, 28,49,51,52]. Here, we apply the proposed model to understand the interplay between temperature and other key factors in CV measurements. Again, the boundary conditions (2.21) with the surface potential given by the scheme (2.22) are prescribed with the Poisson's equation. Fig. 7(a) presents a 3D evolution curve of the charge current in the bulk $j_{o}(0,t)$, the electrostatic surface potential $\phi_{s}(t)$, and the temperature change ΔT compared to the initial temperature at electrodes, in several periods of charging and discharging. In contrast to the traditional plot of current-versus-potential, such a CVT presentation includes the temperature as another player and unravels the dependence of the temperature on both the charge current and surface potential. Overall, one can observe that the temperature rises in a spiral path. It is clearly seen that the temperature rises significantly and linearly after the charge current climbs over its peak value, and remains unchanged in the transitions between charging and discharging processes.

To further understand the pairwise interplay between two of three factors, the CVT evolution curve is projected to the $\phi_s - \Delta T$ plane, $\phi_s - j_{\varrho}$ plane, and $j_a - \Delta T$ plane in Fig. 7. The dependence of ΔT on ϕ_s shows clear alternation between increasing and switching back, with a net increase about 0.003 K in each cycle. The magnitude is smaller than reported experimental data for commercial EDLCs [5,17,24,53]. There are several possible reasons for the discrepancy, e.g., simple planar geometry rather than porous structures is employed in the model. The projection onto the ϕ_s – j_ρ plane gives a typical CV curve that is often shown in CV simulations. It should be pointed out that the projection of the 3D curve of several cycles almost collapse into one overlapped CV curve, indicating that the rising of temperature does not impact the CV simulations very much. One possible reason is that the diffusion coefficient, dielectric coefficient, etc. are assumed to be independent of temperature in the model. Further refinement of our model on this respect should be considered in future work. In addition, the CV curve depicts that the current rises drastically in the initial short period of time. After reaching the peak value, the current declines gradually until it transits from charging process to the discharging process. The peak value can be explained by the formation of a saturation layer in the EDL [49]. The dependence of ΔT on j_a further confirms our finding that the temperature only changes significantly when the charge current is large and has no variation during the charging-discharging transitions.

In order to further probe the CV measurements, we perform simulations with different scan rates and ionic sizes. Fig. 8(a) displays the CV diagram with $\psi_{max}=40k_BT_0/e,~a=0.68nm$, and scan rates ranging from $\nu=1.0\times10^4$ V/s to $\nu=1\times10^5$ V/s. With faster scan

rates, the range for charge current in the charging-discharging process becomes much larger. Also, it is known that the enclosed area of the CV curve represents the charge per unit surface area accumulated at the electrode surface during one cycle [49]. Thus, faster scan rates gives larger integral capacitance for EDLCs in CV measurements. Fig. 8(b) presents the dependence of the counterion concentration at electrodes on the surface potential. Of interest is that, as the scan rate increases, the charging and discharging processes follow different pathways, exhibiting a hysteresis diagram. When the system relaxation time scale is much larger than that of scanning potential, i.e. $\tau_{RC} \gg \tau_{cv}$, the thermal electrokinetics in EDLCs cannot follow the change of scanning potential and the concentration show obvious delayed dynamics. Starting from the second cycle, the discharging stage ends before the concentration relaxes to the bulk concentration 1 M. The retard concentration keeps declining a little bit even though the potential is increasing in the beginning of the next charging stage. This is confirmed by the inset plot of the surface potential and counterion concentration against time. It is reasonable to see that the delayed dynamics becomes less obvious for a slower scan rate $v = 1.0 \times 10^4 \text{ V/s}$, for which $\tau_{RC}/\tau_{cv} \sim \mathcal{O}(1)$. The corresponding concentration relaxes closer to the bulk concentration at the charging-discharging transition.

Fig. 8(c) and (d) present the CV simulations with a fast scan rate $v=1\times10^5~{\rm V/s}$ and three different ionic sizes ranging from $a=0.6~{\rm nm}$ to $a=0.68~{\rm nm}$. With a small ionic size, the range of charge current enlarges, being consistent with the understanding that the maximum value (hump) in the curve is due to the formation of a saturation layer in the EDL [49]. Therefore, a larger area is enclosed by the CV curve and higher integral capacitance is achieved in the CV simulations with a smaller ionic size. The counterion concentration at the electrode shown in Fig. 8(d) demonstrates that, with a smaller ionic size, the saturation concentration increases and the area enclosed by the hysteresis-loop curve gets larger as well. This can be ascribed to the fact that more counterions are involved in the periodic formation and dissolution of the EDLs.

4. Conclusions

This study has proposed a new variational, thermodynamically consistent model to predict thermal electrokinetics in EDLCs by using an energetic variational approach. Modified Nernst–Planck (NP) equations incorporating the diffusion, ionic steric effect, and convection due to the gradient of temperature and electrostatic potential have been developed by using the least action principle and maximum dissipation principle. The proposed modified NP equations are a thermodynamically consistent generalization of the steric NP equations presented in [34] to non-isothermal scenarios with temperature inhomogeneity. Temperature evolution equations with heat source due to thermal pressure and electrostatic interactions have been derived by using laws of thermodynamics.

Extensive simulations of EDLCs have demonstrated that the developed model can successfully predict temperature oscillation in the charging-discharging processes, and larger ionic sizes and faster scan rate of surface potential lead to faster oscillatory temperature rise. In addition, the temperature rise slope, reflecting the irreversible Joule heating effect, has been found to scale quadratically with the average current in cyclic voltammetry (CV). Further study on heat generation source terms have unraveled that they are both exothermic and endothermic in charging and discharging stages, respectively. The discrepancy of source terms in charging and discharging stages, due to irreversible heat generation, gets larger as the scan rate increases. In CV measurements, the temperature has been included as an additional dimension to the traditional CV curve, resulting in a 3D spiral CVT curve. For fast scan rates, the CV curves and counterion concentrations have evidenced that the thermal electrokinetics in EDLCs cannot follow the scanning potential in time, showing delayed dynamics with hysteresis diagrams. Such simulation results have demonstrated that

the proposed model is capable of predicting thermal electrokinetics in EDLCs during charging/discharging processes. With further refinement on the description of porous structure of electrodes and temperature dependent parameters, the proposed model is expected to provide a useful tool for the design, optimization, and manufacture of EDLCs with safety and long-term stability.

CRediT authorship contribution statement

Xiang Ji: Methodology, Investigation, Writing, Visualization. Chun Liu: Conceptualization, Methodology. Pei Liu: Conceptualization, Methodology, Investigation, Writing. Shenggao Zhou: Conceptualization, Methodology, Investigation, Writing, Supervision.

Declaration of competing interest

The authors declare that they have no known competing financial interests or personal relationships that could have appeared to influence the work reported in this paper.

Data availability

Data will be made available on request.

Acknowledgments

C. Liu's work is partially supported by NSF grants DMS-1950868 and DMS-2118181. P. Liu's work is partially supported by NSF grants DMS-1816740. S. Zhou's work is partially supported by the National Natural Science Foundation of China 12171319, Natural Science Foundation of Jiangsu Province (BK20200098), China, Young Elite Scientist Sponsorship Program by Jiangsu Association for Science and Technology, and Shanghai Science and Technology Commission, China (21JC1403700).

Appendix A. Supplementary data

Supplementary material related to this article can be found online at https://doi.org/10.1016/j.jpowsour.2022.232184.

References

- [1] T.F. Fuller, J.N. Harb, Electrochemical Engineering, first ed., Wiley, 2018.
- [2] B. Conway, Electrochemical Supercapacitors: Scientific Fundamentals and Technological Applications, Kluwer Academic/Plenum Publishers, New York, 1999.
- [3] Y. Xu, Z. Lin, X. Zhong, X. Huang, N. Weiss, Y. Huang, X. Duan, Holey graphene frameworks for highly efficient capacitive energy storage, Nature Commun. 5 (2014) 4554.
- [4] X. Yang, C. Chi, Y. Wang, Q. Ling, D. Li, Liquid-mediated dense integration of graphene materials for compact capacitive energy storage, Science 341 (2013) 534–537.
- [5] J. Schiffer, D. Linzen, D. Sauer, Heat generation in double layer capacitors, J. Power Sources 160 (1) (2006) 765–772.
- [6] I. Atlas, G.Z. Ramon, Periodic energy conversion in an electric-double-layer capacitor, J. Colloid Interface Sci. 530 (2018) 675–685.
- [7] A. Burke, Ultracapacitors: why, how, and where is the technology, J. Power Sources 91 (1) (2000) 37–50.
- [8] J. Miller, Electrochemical capacitor thermal management issues at high-rate cycling, Electrochim. Acta 52 (2006) 1703–1708.
- [9] G. Xiong, A. Kundu, T. Fisher, Thermal modeling of supercapacitors, in: Thermal Effects in Supercapacitors, Springer International Publishing, Cham, 2015, pp. 115–141.
- [10] M. Sakka, H. Gualous, J. Mierlo, H. Culcu, Thermal modeling and heat management of supercapacitor modules for vehicle applications, J. Power Sources 194 (2009) 581–587.
- [11] P. Guillemet, Y. Scudeller, T. Brousse, Multi-level reduced-order thermal modeling of electrochemical capacitors, J. Power Sources 157 (2006) 630–640.
- [12] D. Torregrossa, M. Paolone, Modelling of current and temperature effects on supercapacitors ageing. Part I: Review of driving phenomenology, J. Energy Storage 5 (2016) 85–94.

- [13] D. Torregrossa, M. Paolone, Modelling of current and temperature effects on supercapacitors ageing. Part II: State-of-health assessment, J. Energy Storage 5 (2016) 95-101.
- [14] C. Masarapu, H. Zeng, K. Hung, B. Wei, Effect of temperature on the capacitance of carbon nanotube supercapacitors. ACS Nano 3 (2009) 2199–2206.
- [15] C. Pascot, Y. Dandeville, Y. Scudeller, P. Guillemet, T. Brousse, Calorimetric measurement of the heat generated by a double-layer capacitor cell under cycling, Thermochim. Acta 510 (1) (2010) 53–60.
- [16] Y. Dandeville, P. Guillemet, Y. Scudeller, O. Crosnier, L. Athouel, T. Brousse, Measuring time-dependent heat profiles of aqueous electrochemical capacitors under cycling, Thermochim. Acta 526 (1) (2011) 1–8.
- [17] X. Zhang, W. Wang, J. Lu, L. Hua, J. Heng, Reversible heat of electric double-layer capacitors during galvanostatic charging and discharging cycles, Thermochim. Acta 636 (2016) 1–10.
- [18] H. Gualous, H. Louahlia-Gualous, R. Gallay, A. Miraoui, Supercapacitor thermal modeling and characterization in transient state for industrial applications, IEEE Trans. Ind. Appl. 45 (3) (2009) 1035–1044.
- [19] H. Gualous, H. Louahlia, R. Gallay, Supercapacitor characterization and thermal modelling with reversible and irreversible heat effect, IEEE Trans. Power Electron. 26 (11) (2011) 3402–3409.
- [20] O. Bohlen, J. Kowal, D. Sauer, Ageing behaviour of electrochemical double layer capacitors: Part II. Lifetime simulation model for dynamic applications, J. Power Sources 173 (1) (2007) 626–632.
- [21] S. Porras, E. Marziali, B. Gas, E. Kenndler, Influence of solvent on temperature and thermal peak broadening in capillary zone electrophoresis, Electrophoresis 24 (10) (2003) 1553–1564.
- [22] A.L. d'Entremont, L. Pilon, Thermal effects of asymmetric electrolytes in electric double layer capacitors, J. Power Sources 273 (2015) 196–209.
- [23] M. Janssen, R. van Roij, Reversible heating in electric double layer capacitors, Phys. Rev. Lett. 118 (2017) 096001
- [24] A.L. d'Entremont, L. Pilon, First-principles thermal modeling of electric double layer capacitors under constant-current cycling, J. Power Sources 246 (2014) 887–898
- [25] A.L. d'Entremont, L. Pilon, Scaling laws for heat generation and temperature oscillations in edlcs under galvanostatic cycling, Int. J. Heat Mass Transfer 75 (2014) 637-649.
- [26] F. Glatzel, M. Janssen, A. Härtel, Reversible heat production during electric double layer buildup depends sensitively on the electrolyte and its reservoir, J. Chem. Phys. 154 (6) (2021) 064901.
- [27] H. Girard, B. Dunn, L. Pilon, Simulations and interpretation of three-electrode cyclic voltammograms of pseudocapacitive electrodes, Electrochim. Acta 211 (2016) 420–429.
- [28] B. Mei, L. Pilon, Three-dimensional cyclic voltammetry simulations of EDLC electrodes made of ordered carbon spheres, Electrochim. Acta 255 (2017) 160-170.
- [29] C. Lian, M. Janssen, H. Liu, R. van Roij, Blessing and curse: How a supercapacitor's large capacitance causes its slow charging, Phys. Rev. Lett. 124 (2020) 076001
- [30] A. Kundu, L. Pilon, T. Fisher, A continuum model of heat transfer in electrical double-layer capacitors with porous electrodes under constant-current cycling, J. Power Sources 511 (2021) 230404
- [31] J. Yang, M. Janssen, C. Lian, R. van Roij, Simulating the charging of cylindrical electrolyte-filled pores with the modified Poisson-Nernst-Planck equations, J. Chem. Phys. 156 (21) (2022) 214105.

- [32] Y. Lin, C. Lian, M. Berrueta, H. Liu, R. van Roij, Microscopic model for cyclic voltammetry of porous electrodes, Phys. Rev. Lett. 126 (2022) 206001.
- [33] P. Huang, H. Tao, J. Yang, C. Lian, H. Liu, Four stages of thermal effect coupled with ion-charge transports during the charging process of porous electrodes, AIChE, J. (2022).
- [34] M.S. Kilic, M. Bazant, A. Ajdari, Steric effects in the dynamics of electrolytes at large applied voltages. II. Modified Poisson–Nernst–Planck equations, Phys. Rev. E 75 (2007) 021503.
- [35] S. Zhou, Z. Wang, B. Li, Mean-field description of ionic size effects with non-uniform ionic sizes: A numerical approach, Phys. Rev. E 84 (2011) 021901.
- [36] B. Li, P. Liu, Z. Xu, S. Zhou, Ionic size effects: generalized Boltzmann distributions, counterion stratification, and modified debye length, Nonlinearity 26 (10) (2013) 2899.
- [37] X. Ji, S. Zhou, Variational approach to concentration dependent dielectrics with the Bruggeman model: Theory and numerics, Commun. Math. Sci. 17 (7) (2019) 1949–1974.
- [38] C. Liu, An Introduction of Elastic Complex Fluids: An Energetic Variational Approach, 2009, pp. 286–337.
- [39] C. Liu, H. Sun, On energetic variational approaches in modeling the nematic liquid crystal flows, Discrete Contin. Dyn. Syst. 23 (2009) 455–475.
- [40] C. Liu, J. Shen, A phase field model for the mixture of two incompressible fluids and its approximation by a Fourier-spectral method, Physica D 179 (2003) 211–228
- [41] B. Eisenberg, Y. Hyon, C. Liu, Energy variational analysis of ions in water and channels: Field theory for primitive models of complex ionic fluids, J. Chem. Phys. 133 (2010) 104104.
- [42] I. Borukhov, D. Andelman, H. Orland, Steric effects in electrolytes: A modified Poisson–Boltzmann equation, Phys. Rev. Lett. 79 (1997) 435–438.
- [43] M.S. Kilic, M. Bazant, A. Ajdari, Steric effects in the dynamics of electrolytes at large applied voltages. I. Double-layer charging, Phys. Rev. E 75 (2007) 021502.
- [44] S. Xu, P. Sheng, C. Liu, An energetic variational approach for ion transport, Commun. Math. Sci. 12 (2014) 779–789.
- [45] P. Liu, S. Wu, C. Liu, Non-isothermal electrokinetics: Energetic variational approach, Commun. Math. Sci. 16 (5) (2018) 1451–1463.
- [46] J. Forster, Mathematical Modeling of Complex Fluids (Master thesis), University of Würzburg, 2013.
- [47] A. Majee, A. Würger, Collective thermoelectrophoresis of charged colloids, Phys. Rev. E 83 (2011) 061403.
- [48] R. Stout, A. Khair, Diffuse charge dynamics in ionic thermoelectrochemical systems, Phys. Rev. E 96 (2017) 022604.
- [49] H. Wang, L. Pilon, Physical interpretation of cyclic voltammetry for measuring electric double layer capacitances. Electrochim. Acta 64 (2012) 130–139.
- [50] J. Kierzenka, L. Shampine, A BVP solver based on residual control and the Matlab PSE, ACM Trans. Math. Software 27 (2001) 299–316.
- [51] H. Girard, H. Wang, A.L. d'Entremont, L. Pilon, Physical interpretation of cyclic voltammetry for hybrid pseudocapacitors, J. Phys. Chem. C 119 (2015) 11349–11361.
- [52] H. Wang, A. Thiele, L. Pilon, Simulations of cyclic voltammetry for electric double layers in asymmetric electrolytes: A generalized modified Poisson-Nernst-Planck model, J. Phys. Chem. C 117 (2013) 18286–18297.
- [53] Y. Parvini, J. Siegel, A. Stefanopoulou, A. Vahidi, Supercapacitor electrical and thermal modeling, identification, and validation for a wide range of temperature and power applications, IEEE Trans. Ind. Electron. 63 (3) (2016) 1574–1585.